Check for updates

Novel spinel-type selenide semiconductor ZnSc$_2$Se$_4$ and its solid solution with sulfide for photovoltaics

Kota Hanzawa, [ID] [a] Ryoga Nagasawa[a] and Hidenori Hiramatsu *[ab]

It has recently been reported that the spinel-type sulfide $(Zn,Mg)Sc_2S_4$ possesses optoelectronic properties, including both n- and p-type dopability and strong visible-light emission. Herein, we present a novel isomorphic selenide, $ZnSc_2Se_4$, synthesized using a high-pressure synthesis technique, which exhibits n-type semiconducting behavior. Additionally, a solid solution between $ZnSc_2S_4$ and $ZnSc_2Se_4$ is realized over the entire composition range, enabling continuous tuning of the direct optical band gap from 2.07 to 1.35 eV (visible to near-infrared) by adjusting the S/Se ratio, accompanied by a sharp enhancement in electrical conductivity. These results revealed that the spinel-type chalcogenide system is a highly promising platform for photovoltaic absorbers. Furthermore, by substituting isovalent Mg $[(Zn_{1-z}Mg_z)Sc_2(S_{1-x}Se_x)_4]$, the band gap can be precisely controlled across nearly the entire visible region (2.86–1.35 eV), providing additional tunability for high-efficiency light-absorption and emission applications within the same host lattice.

New concepts

This paper offers a novel promising candidate for optoelectronic semiconductors possessing a suitable direct band gap for photovoltaic applications through materials exploration based on an original design concept. Following this concept, we recently validated that spinel-type $ZnSc_2S_4$ has ambipolar (both n- and p-type) conductivity and a direct band gap essential for optoelectronics. However, its band gap (2.07 eV) is excessively wide for optimal photovoltaic absorption. This challenge motivated the pursuit of its selenide counterpart, $ZnSc_2Se_4$, which has remained experimentally unreported. Here, we report the first-ever synthesis of $ZnSc_2Se_4$ using a high-pressure technique, revealing it to be an n-type semiconductor with a direct near-infrared band gap (1.35 eV). Furthermore, we demonstrate that a solid solution over the entire composition range, $ZnSc_2(S_{1-x}Se_x)_4$, unlocks continuous band gap tunability from the near-infrared to the visible region. This discovery establishes spinel-type chalcogenides as a new platform offering band gap engineering; by incorporating Mg, the $(Zn_{1-z}Mg_z)Sc_2(S_{1-x}Se_x)_4$ system can span nearly the entire visible spectrum (1.35–2.86 eV), creating a highly versatile material system for next-generation optoelectronics.

Introduction

Photovoltaic technologies are essential for resolving current energy challenges and realizing a low-carbon society. Although commercial solar cells are predominantly manufactured from Si, its indirect band gap imposes a low absorption coefficient, thereby restricting the device structure.[1] Therefore, alternative materials have been desired. Representative candidates,[2] such as chalcogenides (*e.g.*, CdTe[3] and $Cu(In,Ga)Se_2$[4]) and pnictide semiconductors (*e.g.*, GaAs[5]), exhibit high power conversion efficiencies exceeding 20% in solar cell devices. Furthermore, halide perovskite solar cells have recently attracted significant attention and currently surpass 25% efficiency,[6] making them promising candidates for next-generation photovoltaic applications such as flexible modules and high-performance tandem cells with Si. However, halide perovskites face critical issues related to their long-term stability and the use of Pb,[7] which complicate their durability and compliance with international environmental regulations, such as the Restriction of Hazardous Substances (RoHS). These challenges have motivated the ongoing exploration of novel optoelectronic semiconductors.

Tremendous efforts have been devoted to exploring alternative candidate materials,[8] including oxides (*e.g.*, Cu_2O[9]), nitrides (*e.g.*, $ZnSnN_2$,[10] $CaZn_2N_2$,[11–13] and Cu_3N[14]), pnictides (*e.g.*, $ZnSnP_2$[15]), and chalcogenides (*e.g.*, $Cu_2ZnSnS_{4-x}Se_x$,[16] SnS,[17] and $BaZrS_3$[18–21]). Nevertheless, stringent requirements for these candidates, which must at least possess superior optical properties with a direct transition-type band gap suitable for photoabsorption, as well as outstanding electronic transport characteristics on n- and p-type conduction for the construction of homo-pn junctions, have impeded efficient novel materials exploration. To accelerate this exploration,

[a] *Materials and Structures Laboratory, Institute of Integrated Research, Institute of Science Tokyo, 4259 Nagatsuta, Midori, Yokohama 226-8501, Japan.*
E-mail: hiramatsu.h.aa@m.titech.ac.jp

[b] *MDX Research Center for Element Strategy, Institute of Integrated Research, Institute of Science Tokyo, 4259 Nagatsuta, Midori, Yokohama 226-8501, Japan*

robust materials design concepts are necessary. To date, we have proposed concepts for designing optoelectronic semiconductors with direct band gaps suitable for optoelectronics and appropriate energy levels for both n- and p-type carrier doping. For example, in perovskite-type sulfides, we established a concept based on nonbonding states that yield a deep conduction band minimum (CBM) and a shallow valence band maximum (VBM) relative to the vacuum level and band folding that produces a direct band gap.[22] Experimentally, it was demonstrated that $SrHfS_3$[22] and $BaZrS_3$[19–23] exhibit superior carrier controllability for both n- and p-type conduction and high optical responses, including intense emission and extraordinarily high absorption coefficients ($>10^5$ cm^{-1}) at band gaps suitable for use in Si-tandem solar cells. Furthermore, a novel concept was recently developed based on chemical bonding and atomic orbital symmetry for the spinel-type chalcogenides AB_2Ch_4 (Ch = S, Se, and Te),[24] which were engineered to enable both n- and p-type doping by designing a CBM derived from the deep s^0 orbitals of a heavy A-site cation and a VBM arising from shallow nonbonding Ch p orbitals. In addition, even though AB_2Ch_4 with an s^0 cation at the B site has an indirect band gap, by adopting a d^0 cation that contributes to strong interactions with the p orbitals of Ch in this system compared with the s^0 one, energy bands near the VBM are pushed down around specific zone boundaries, resulting in a direct-band gap structure. These factors contribute to the simultaneous realization of direct optical transitions and dopability. Following this concept, a spinel-type sulfide, $ZnSc_2S_4$, was experimentally demonstrated to exhibit intense visible emission widely tunable from 2.07 to 2.86 eV via isovalent Mg substitution at the Zn site as well as both n- and p-type carrier controllability over nine orders of magnitude in conductivity from the intrinsic level (10^{-11} S cm^{-1}) to the semiconducting one (10^{-2} S cm^{-1}) through chemical doping and intentional introduction of defects.[24] These results indicate that spinel-type chalcogenides possessing the abovementioned electronic structures hold high potential for optoelectronics. However, a challenge arises in extending spinel-type sulfides as photoabsorber materials in solar cells: they have wider band gaps than the optimum gaps predicted using the Shockley–Queisser limit[25] for achieving efficient photovoltaics. Our electronic structure calculations for the spinel-type sulfides revealed that there are potential candidates, such as ZnY_2S_4 (calculated band gap = 1.45 eV[24]), with a band gap slightly narrower than that of $ZnSc_2S_4$ (1.50 eV[24]); however, the deviation is as low as 0.05 eV. This indicates that no spinel-type sulfides offer direct band gaps that match the limit. Hence, we considered that the substitution of Se at the S site in $ZnSc_2S_4$ is essential to effectively reduce the gap, where the hybridization of the shallower Se 4p orbitals should raise the VBM level. However, the corresponding counterpart, $ZnSc_2Se_4$, has not yet been reported experimentally, even though the electronic structures have been investigated using first-principles density functional theory calculations.[26]

In this study, we synthesize a novel spinel-type selenide, $ZnSc_2Se_4$, using a high-pressure synthesis technique and examine its optoelectronic properties through the formation of a solid solution between $ZnSc_2S_4$ and $ZnSc_2Se_4$. Consequently, we demonstrate that spinel-type $ZnSc_2Se_4$ is an intrinsic n-type semiconductor with a widely tunable band gap from 1.35 eV to 2.07 eV by anion substitution. This result widely expands the potential for optoelectronic applications via a combination of isovalent Mg substitution, because the band gap can be tuned over the entire visible wavelength region from 2.86 to 1.35 eV in $(Zn,Mg)Sc_2(S,Se)_4$.

Results and discussion

Prior to substituting Se into $ZnSc_2S_4$, we investigated whether the other end-member, spinel-type $ZnSc_2Se_4$, was thermodynamically stable and could be synthesized, because it was experimentally unreported. We first attempted to synthesize $ZnSc_2Se_4$ via a conventional solid-state reaction at ambient pressure (AP), analogous to $ZnSc_2S_4$ synthesis.[24] The bottom of Fig. 1a shows the powder X-ray diffraction (XRD) pattern of the obtained sample. The major diffraction peaks were indexed to diffraction from spinel-type $ZnSc_2Se_4$ by using an initial crystal structure model of $ZnSc_2S_4$ with the space group $Fd\bar{3}m$; impurity phases assigned to the ZnSe and Sc_2Se_3 precursors were also detected, suggesting that spinel-type $ZnSc_2Se_4$ thermodynamically competes with these precursors under AP growth conditions. To suppress impurity segregation, we adopted a high-pressure synthesis because it was expected that external pressure would lower the activation barriers and promote kinetically hindered reactions. The middle and top of Fig. 1a show the XRD patterns of samples synthesized at high pressures (P) of 1.5 and 5.0 GPa, respectively. With increasing P, the diffraction intensity of the Sc_2Se_3 phase decreases. Fig. 1b summarizes the relationship between P and the mole fractions of the observed phases. Although the mole fraction of $ZnSc_2Se_4$ was as low as 48% under AP, it increased with P and reached 67% at 5.0 GPa, which was accompanied by a significant decrease in the Sc_2Se_3 fraction to zero. This indicates that the external pressure effectively stabilized the $ZnSc_2Se_4$ phase. In contrast, the fraction of ZnSe was nearly independent of P, and excess ZnSe remained in the sample irrespective of the stoichiometric mixture of the starting precursors. Therefore, we tuned the nominal starting precursor ratio, y = ZnSe/Sc_2Se_3, to suppress ZnSe segregation. Fig. 1c shows the variations in the mole fractions of $ZnSc_2Se_4$ and ZnSe as a function of y for the samples synthesized at 5.0 GPa. As expected, the ZnSe fraction decreased continuously with decreasing y, and correspondingly, the $ZnSc_2Se_4$ fraction increased. Consequently, at y = 0.5, single-phase $ZnSc_2Se_4$ was successfully obtained. The chemical composition was evaluated using an electron probe micro analyzer (EPMA). Fig. S1 shows the electron micrograph obtained using the EPMA, confirming that no impurity phases exist. However, it was also clarified that the $ZnSc_2Se_4$ grain has an Sc- and Se-rich chemical composition, which may suggest that excess Sc_2Se_3 in the nominal precursors forms nano-sized amorphous phases that cannot be detected by XRD. The XRD pattern of single-phase $ZnSc_2Se_4$ is shown in Fig. 1d. Because
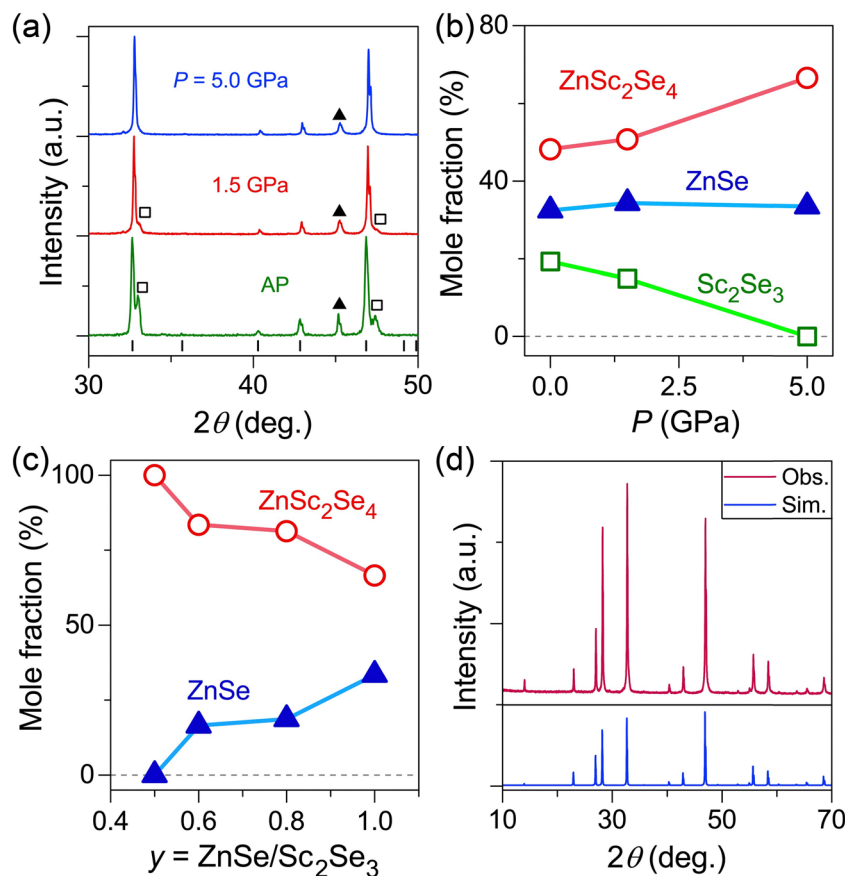
Fig. 1 Structural analyses of the samples synthesized by solid-state reactions between ZnSe and Sc_2Se_3 precursors. (a) Powder XRD patterns of the samples synthesized at ambient pressure (AP) and under external pressures (P) of 1.5 and 5.0 GPa. Vertical black bars at the bottom in (a) indicate the diffraction angles of spinel-type $ZnSc_2Se_4$, calculated using the crystal structure of $ZnSc_2S_4$ as an initial model. Solid triangles and open squares denote diffractions from the impurity phases ZnSe and Sc_2Se_3, respectively. (b) Mole fraction of the obtained phases in (a) as a function of P. (c) Nominal precursor ratio y (= $ZnSe/Sc_2Se_3$) dependence of the mole fraction on the samples synthesized at P = 5.0 GPa. (d) Powder XRD pattern of the obtained single-phase $ZnSc_2Se_4$ (top) with a simulated diffraction pattern (bottom).

the observed pattern was well reproduced by the simulated profile based on the spinel-type structure model, it was concluded that $ZnSc_2Se_4$ was a novel spinel-type compound.

We then calculated the electronic structure of spinel-type $ZnSc_2Se_4$. The band structure and the corresponding partial and total densities of states (DOS) are shown in Fig. 2a and b,
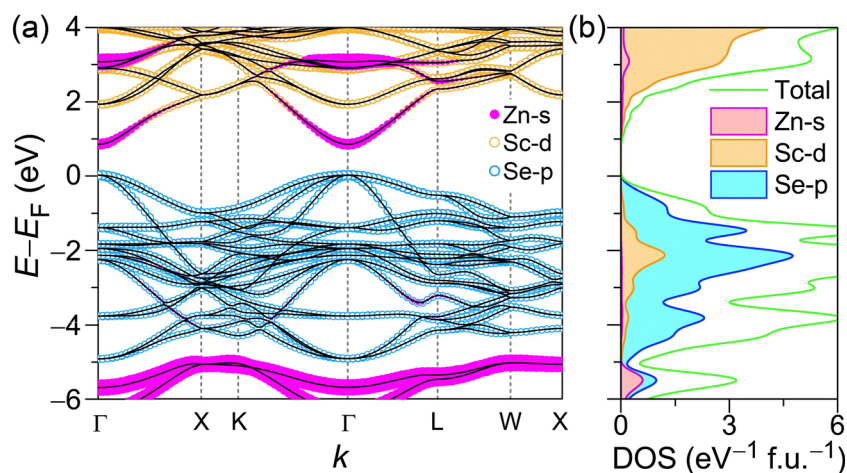

Fig. 2 Electronic structure of spinel-type $ZnSc_2Se_4$. (a) Band structure with contributions of Zn-s (solid pink circles), Sc-d (open orange), and S-p (open light blue) orbitals. (b) Partial density of states (DOS) for Zn-s (pink), Sc-d (orange), and Se-p (light blue) orbitals and total DOS (green).

respectively. Similar to $ZnSc_2S_4$, in which the CBM and VBM are mainly composed of Zn-s and S-p orbitals at the Γ point, $ZnSc_2Se_4$ also has a direct band gap formed by Zn-s for the CBM and Se-p for the VBM. This result is consistent with our design concept for realizing direct-gap spinel-type semiconductors.[24] The calculated band gap (E_g) is 0.83 eV, which is narrower than that of $ZnSc_2S_4$[24] owing to the shallower energy level of Se 4p orbitals relative to that of S 3p. Because both $ZnSc_2S_4$ and $ZnSc_2Se_4$ possess the same spinel-type crystal structure and direct band gaps, E_g should be tunable from the near-infrared to the visible region across a suitable wavelength range for an absorber layer in photovoltaic applications by forming a solid solution between them.

To experimentally validate E_g tunability, we synthesized continuously Se-substituted $ZnSc_2S_4$, that is, $ZnSc_2(S_{1-x}Se_x)_4$ ($x = 0$–1), *via* a solid-state reaction between both end members. Fig. 3a shows the XRD patterns of $ZnSc_2(S_{1-x}Se_x)_4$ as a function of x, where the main phase of all the samples was identified to be the spinel-type structure. Since some samples contained impurity phases, which may originate from crystallization of the nano-sized Sc–Se amorphous phase during thermal annealing and/or partial decomposition of $ZnSc_2(S_{1-x}Se_x)_4$, their precise chemical compositions could not be directly determined by chemical analysis. Therefore, x was defined based on the Rietveld refinement results (see Fig. S2 and Tables S1, S2 for the fitting results). The continuous peak shift in Fig. 3a with

increasing x indicates that the *a*-axis lattice parameter (a) expands linearly, as shown in Fig. 3b. Because this expansion originated from the substitution of S by Se with a larger ionic radius, it was concluded that the S sites in $ZnSc_2S_4$ could be replaced by Se over the entire x range, that is, successful fabrication of the solid solution. Along with the lattice expansion, the Sc–*Ch* and Zn–*Ch* bond lengths increase from 2.569 ($x = 0$) to 2.695 Å ($x = 1$) and from 2.366 to 2.440 Å, respectively (Fig. 3c). By comparing these with ionic bond lengths, which are estimated by summing the ionic radii of the cations [Sc (0.87 Å) or Zn (0.64 Å)] and anions [S (1.70 Å) or Se (1.84 Å)] while accounting for a degree of covalency,[27] it was revealed that the observed Sc–*Ch* distances are nearly identical to the ideal ones, where the differences are approximately 0.02 Å. In contrast, clear deviations were observed for the Zn–*Ch* bonds. The observed Zn–S length (2.366 Å) differs from the estimated one (2.34 Å) by 0.026 Å, and the deviation further increases to 0.04 Å in $ZnSc_2Se_4$. This suggests that the Zn site incorporates a deficiency and/or static disorder (*e.g.*, anti-site defects such as Sc on the Zn site), and these effects are enhanced with increasing fitted x. This speculation is supported by the refined isotropic displacement parameters (B) in Table S1, where B values at the Zn site are unusually large and increase with increasing fitted x, because B is strongly correlated with site occupancy and static disorder. Fig. 3d shows the relationship between x and the *Ch*–Sc–*Ch*
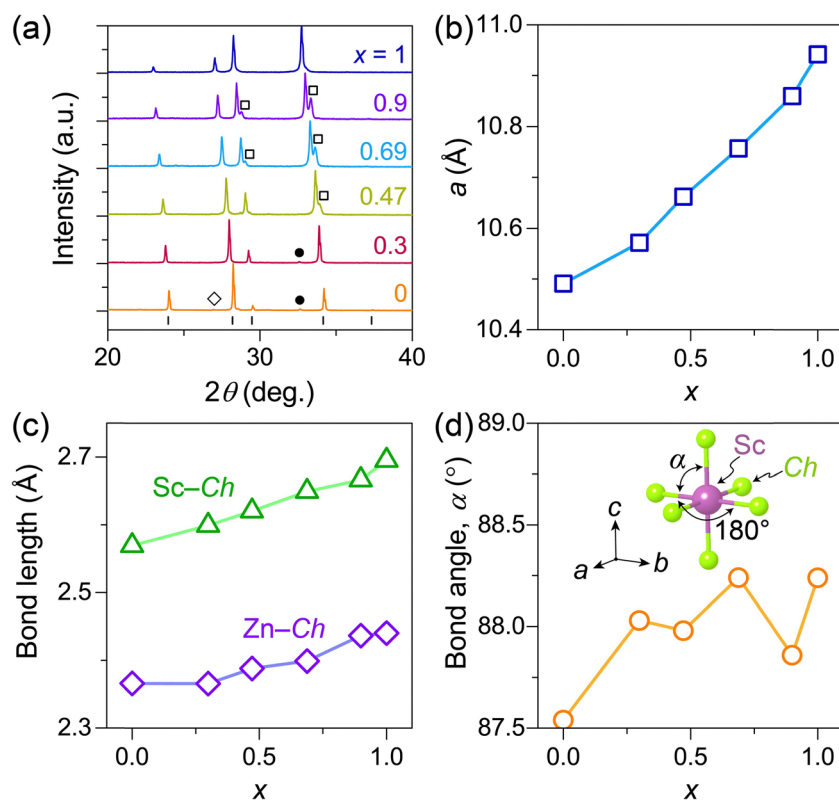

Fig. 3 Structural analyses of spinel-type $ZnSc_2(S_{1-x}Se_x)_4$. (a) Powder XRD patterns of the $x = 0$–1 samples. Vertical black bars at the bottom indicate the diffraction angles of $ZnSc_2S_4$. Squares, diamonds, and solid circles represent diffraction peaks from the impurity phases Sc_2Se_3, ZnS, and Sc_2O_2S, respectively. (b) x dependence of the *a*-axis lattice parameter (a). (c) Variation of bond lengths between Sc and *Ch* (*Ch* = S and/or Se, green), and Zn and *Ch* (purple) with increasing x. (d) Relationship between x and the bond angle (α) of *Ch*–Sc–*Ch* in Sc*Ch*$_6$ octahedra, which is shown in the inset.

bond angle (α) in ScCh_6 octahedra; the Ch–Zn–Ch angle in ZnCh_4 tetrahedra remains constant at 109.47° (the angle of an isotropic tetrahedron) for all x. With increasing x, α slightly increases toward 90°, which is associated with a change in the tolerance factor $\left[\sqrt{3}(R_B + R_X)/2((R_A + R_X)),\right.$ where $R_B + R_X$ and $R_A + R_X$ are the Sc–Ch and Zn–Ch bond lengths, and the ideal numerical value is around 1$\left.\right]^{28}$ from 0.94 ($x = 0$) to 0.96 ($x = 1$).

Next, we evaluated the optical properties of the $x = 0$–1 samples. Fig. 4a shows Tauc plots as functions of x. The E_g value of the $x = 1$ sample (ZnSc$_2$Se$_4$) was determined to be 1.35 eV. Moreover, it was unveiled that E_g is continuously tunable from 2.07 eV at $x = 0$ to 1.35 eV at $x = 1$ by varying x, owing to the combination of S and Se p orbitals. This wide tuning range of E_g confirms that ZnSc$_2$(S$_{1-x}$Se$_x$)$_4$ is suitable as an absorber for both single-junction and tandem solar cells according to the Shockley–Queisser limit.[25] Fig. 4c shows normalized photoluminescence (PL) spectra measured at room temperature (RT) for $x = 0$, 0.3, and 1. The PL peak energies shift from 2.07 eV at $x = 0$ to 1.83 eV at $x = 0.3$ and 1.33 eV at $x = 1$. Because these peak energies closely match the E_g values in Fig. 4b, and the PL lifetimes in Figure S3 were shorter than 10 ns, the origin of the PL was concluded to be band-to-band recombination owing to direct band gaps. For other x values, clear PL was not detected at RT, likely because of defect-related nonradiative recombination arising from internal strain and/or relatively low phase purity ($\sim$70%).

To clarify the electronic transport properties, the electrical conductivity (σ) of the $x = 0$–1 samples was evaluated at RT. Fig. 5 plots the x dependence of σ, where $x = 0$ exhibits insulating behavior with a quite low σ of 2.5 × 10^{-11} S cm^{-1}. However, σ increases considerably to the 10^{-9} S cm^{-1} range at $x = 0.3$–0.7 and reaches 1.8 × 10^{-5} S cm^{-1} at $x = 1$, which is a six-order-of-magnitude enhancement. Because these σ values can be affected by scattering at impurity phases in grain boundaries and/ or the nano-sized amorphous phases as speculated above, the preparation of high-quality samples such as epitaxial thin films is expected to result in much superior electronic transport properties. Carrier polarity was investigated by a thermoelectromotive force measurement, where reliable voltage signals were obtained
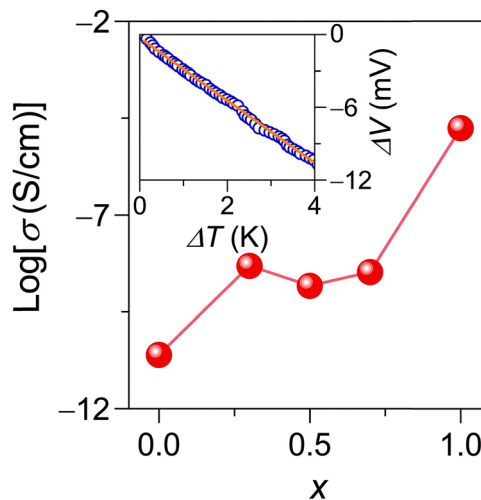

Fig. 5 Electrical conductivities (σ) of ZnSc$_2$(S$_{1-x}$Se$_x$)$_4$ ($x = 0$–1) bulks at room temperature. (inset) Thermoelectromotive force measurement for a ZnSc$_2$Se$_4$ bulk. The solid line in the inset represents the linear least-squares fitting results.

only for $x = 1$, likely due to the low σ of the other x samples. The inset of Fig. 5 presents the plot of ΔV *versus* ΔT for $x = 1$, yielding a clear negative slope with a Seebeck coefficient of -2600 μV K^{-1}. Hence, it can be concluded that undoped ZnSc$_2$Se$_4$ is an n-type semiconductor. Although the origin of the supply of n-type carriers has been unidentified, we speculate that it may be associated with Zn site-related point defects, such as the anti-site defects of Sc on the Zn site, as discussed in the above structural analysis, because of the Sc$_2$Se$_3$-rich high-pressure synthesis conditions ($y = 0.5$). These results highlight the potential of the solid solution ZnSc$_2$(S$_{1-x}$Se$_x$)$_4$ for optoelectronic semiconductors.

Conclusions

In summary, we have demonstrated the optoelectronic properties of the spinel-type chalcogenide solid solution ZnSc$_2$(S$_{1-x}$Se$_x$)$_4$ ($x = 0$–1). Although ZnSc$_2$Se$_4$ had not been
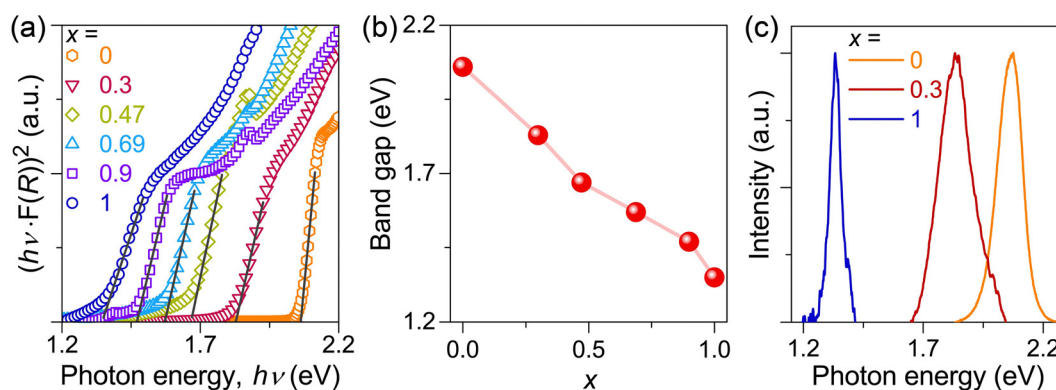

Fig. 4 Optical properties of ZnSc$_2$(S$_{1-x}$Se$_x$)$_4$ ($x = 0$–1). (a) Tauc plots of diffuse reflectance spectra, where solid lines represent the results of least-squares fittings to estimate optical band gaps (E_g). (b) Relationship between x and E_g estimated from (a). (c) Normalized PL spectra measured at room temperature.

experimentally reported, it was successfully synthesized using a high-pressure method. Two key factors are essential for obtaining the single phase: applying a high pressure of 5 GPa and sufficiently reducing the nominal ZnSe content. The direct transition type E_g of the solid solution was continuously tuned from 2.07 to 1.35 eV by controlling x, and band-to-band emission at RT was observed at the corresponding E_g. The σ value at RT significantly increased with increasing x, from 2.5×10^{-11} S cm^{-1} for ZnSc$_2$S$_4$ ($x = 0$) to 1.8×10^{-5} S cm^{-1} for n-type ZnSc$_2$Se$_4$ ($x = 1$). Furthermore, additional substitution of isovalent Mg into the Zn site, $[(Zn_{1-z}Mg_z)Sc_2(S_{1-x}Se_x)_4]$, would enable further band-gap engineering across nearly the entire visible region (2.86–1.35 eV) within the same host spinel-type lattice, paving the way for next-generation high-efficiency photovoltaic absorber layers and light-emitting materials; however, the development of thin film growth processes is essential, because the high-pressure synthesis process is not preferred for practical photovoltaic devices. In addition, solar cells with nano-sized quantum dots as the absorption layer are considered one of the key candidates for third-generation photovoltaics, offering higher efficiency and stronger absorption, with recent intensive research on quantum dots such as PbS,[29] CdSe,[30] and Pb-based perovskite,[31] which have already demonstrated high performance. By employing the spinel-type chalcogenide as an alternative, new toxic-element-free nano-scale quantum dot solar cells with precise band-gap engineering over a wide spectral range may be developed, owing to continuous and wide band-gap tunability *via* solid solutions as well as the quantum size effect.

Experimental

Calculations

The band structure and density of states (DOS) of ZnSc$_2$Se$_4$ were characterized using first-principles density functional theory calculations. In the calculations, the HSE06 hybrid functional,[32] implemented in the Vienna *Ab Initio* Simulation Package (VASP),[33,34] was employed. The cutoff energy was set to 650 eV for all calculations, and the Brillouin zone was sampled using an $8 \times 8 \times 8$ k-point mesh for self-consistent field and DOS calculations.

Synthesis

To synthesize polycrystalline ZnSc$_2$Se$_4$ bulks, conventional solid-state reactions and high-pressure synthesis methods were employed. In the solid-state reaction, the precursor powders of ZnSe and Sc$_2$Se$_3$, prepared by a chemical reaction between Sc metal and Se at 800 °C, were stoichiometrically wet-mixed and then sintered at 1000 °C in evacuated silica glass ampules. The procedure was similar to that of ZnSc$_2$S$_4$, which has been reported in ref. 24. For the high-pressure synthesis, a belt-type anvil was employed, where the same precursors were pressed at 1.5 or 5.0 GPa during heating at 1000 °C for 0.5 h. The precursor ratio (y = ZnSe/Sc$_2$Se$_3$) was tuned to decrease the impurity ZnSe phase fraction at 5.0 GPa. A solid solution of

ZnSc$_2$(S$_{1-x}$Se$_x$)$_4$ (x = 0–1) was fabricated over the entire x range *via* a solid-state reaction between ZnSc$_2$Se$_4$ and ZnSc$_2$S$_4$ at 1000 °C in evacuated silica glass ampules.

Characterization

Characterizations were performed in air owing to the sample stability, except for the photoluminescence (PL) and Seebeck effect measurements, and at room temperature. The crystal structures and phases were characterized by powder X-ray diffraction (XRD) with Cu Kα radiation, and the structural parameters as well as the amounts of impurity phases were evaluated by Rietveld refinement using RIGAKU SmartLab Studio II software. In all Rietveld refinements, the ZnSc$_2$S$_4$ structure (Inorganic Crystal Structure Database (ICSD) code no. 101174) was used as an initial structure model, and as for the atomic position and site occupancy, only the S and Se sites were refined. The pattern simulation in Fig. 1d was performed using the RIETAN-FP code.[35] Electron probe microanalysis (EPMA) with wavelength-dispersive X-ray spectroscopy was employed to evaluate the chemical composition. The optical band gaps (E_g) were estimated *via* the Kubelka–Munk transformation of the diffuse reflectance spectra in the ultraviolet–visible wavelength region. PL of ZnSc$_2$S$_4$ and ZnSc$_2$Se$_4$ bulks was measured with an excitation source of the third-harmonic generation of a Nd:YAG laser (wavelength, λ = 355 nm) in a vacuum, while that of ZnSc$_2$(S$_{0.7}$Se$_{0.3}$)$_4$ was recorded with its second-harmonic generation (532 nm). The PL lifetime was determined using time-resolved PL measurements. The electrical conductivities (σ) of the bulk samples were examined by the four-probe method using approximately 100 nm thick Au contact electrodes. The carrier polarity of ZnScSe$_4$ was determined *via* thermoelectromotive force (Seebeck effect) measurements with a two-probe configuration established using the Au electrode in an Ar atmosphere.

Author contributions

K. H. wrote the manuscript and performed the characterizations. R. N. synthesized the samples. H. H. reviewed the manuscript and supervised the research.

Conflicts of interest

The authors declare no competing financial interests.

Data availability

Acknowledgements

References

1 L. C. Andreani, A. Bozzola, P. Kowalczewski, M. Liscidini and L. Redorici, Silicon solar cells: toward the efficiency limits, *Adv. Phys.: X*, 2019, **4**(1), 1548305, DOI: 10.1080/23746149.2018.1548305.

2 M. A. Green, E. D. Dunlop, M. Yoshita, N. Kopidakis, K. Bothe, G. Siefer, D. Hinken, M. Rauer, J. Hohl-Ebinger and X. Hao, Solar cell efficiency tables (Version 64), *Prog. Photovoltaics Res. Appl.*, 2024, **32**(7), 425–441, DOI: 10.1002/pip.3831.

3 First Solar Press Release, First Solar Builds the Highest Efficiency Thin Film PV Cell on Record, 5 2014.

4 M. Nakamura, K. Yamaguchi, Y. Kimoto, Y. Yasaki, T. Kato and H. Sugimoto, Cd-Free Cu(In,Ga)(Se,S)$_2$ Thin-Film Solar Cell With Record Efficiency of 23.35%, *IEEE J. Photovolt.*, 2019, **9**(6), 1863–1867, DOI: 10.1109/JPHOTOV.2019.2937218.

5 B. M. Kayes, H. Nie, R. Twist, S. G. Spruytte, F. Reinhardt, I. C. Kizilyalli and G. S. Higashi, 27.6% Conversion Efficiency, a New Record for Single-Junction Solar Cells under 1 Sun Illumination, *In 2011 37th IEEE Photovoltaic Specialists Conference*, 2011, pp. 000004–000008, DOI: 10.1109/PVSC.2011.6185831.

6 C. Yang, W. Hu, J. Liu, C. Han, Q. Gao, A. Mei, Y. Zhou, F. Guo and H. Han, Achievements, challenges, and future prospects for industrialization of perovskite solar cells, *Light: Sci. Appl.*, 2024, **13**(1), 227, DOI: 10.1038/s41377-024-01461-x.

7 L. Duan, D. Walter, N. Chang, J. Bullock, D. Kang, S. P. Phang, K. Weber, T. White, D. Macdonald, K. Catchpole and H. Shen, Stability challenges for the commercialization of perovskite–silicon tandem solar cells, *Nat. Rev. Mater.*, 2023, **8**(4), 261–281, DOI: 10.1038/s41578-022-00521-1.

8 A. Zakutayev, J. D. Major, X. Hao, A. Walsh, J. Tang, T. K. Todorov, L. H. Wong and E. Saucedo, Emerging inorganic solar cell efficiency tables (Version 2), *J. Phys. Energy*, 2021, **3**(3), 032003, DOI: 10.1088/2515-7655/abebca.

9 A. Lakshmanan, Z. C. Alex and S. R. Meher, Recent advances in cuprous oxide thin film based photovoltaics, *Mater. Today Sustainability*, 2022, **20**, 100244, DOI: 10.1016/j.mtsust.2022.100244.

10 I. S. Khan, K. N. Heinselman and A. Zakutayev, Review of ZnSnN$_2$ semiconductor material, *J. Phys. Energy*, 2020, **2**(3), 032007, DOI: 10.1088/2515-7655/ab8b69.

11 Y. Hinuma, T. Hatakeyama, Y. Kumagai, L. A. Burton, H. Sato, Y. Muraba, S. Iimura, H. Hiramatsu, I. Tanaka, H. Hosono and F. Oba, Discovery of earth-abundant nitride semiconductors by computational screening and high-pressure synthesis, *Nat. Commun.*, 2016, **7**(1), 11962, DOI: 10.1038/ncomms11962.

12 M. Tsuji, H. Hiramatsu and H. Hosono, Tunable Light Emission through the Range 1.8–3.2 eV and p-Type Conductivity at Room Temperature for Nitride Semiconductors, Ca(Mg$_{1-x}$Zn$_x$)$_2$N$_2$ (x = 0–1), *Inorg. Chem.*, 2019, **58**(18), 12311–12316, DOI: 10.1021/acs.inorgchem.9b01811.

13 M. Tsuji, K. Hanzawa, H. Kinjo, H. Hiramatsu and H. Hosono, Heteroepitaxial Thin-Film Growth of a Ternary Nitride Semiconductor CaZn$_2$N$_2$, *ACS Appl. Electron. Mater.*, 2019, **1**(8), 1433–1438, DOI: 10.1021/acsaelm.9b00248.

14 K. Matsuzaki, K. Harada, Y. Kumagai, S. Koshiya, K. Kimoto, S. Ueda, M. Sasase, A. Maeda, T. Susaki, M. Kitano, F. Oba and H. Hosono, High-Mobility p-Type and n-Type Copper Nitride Semiconductors by Direct Nitriding Synthesis and In Silico Doping Design, *Adv. Mater.*, 2018, **30**(31), 1801968, DOI: 10.1002/adma.201801968.

15 T. Kuwano, R. Katsube, K. Kazumi and Y. Nose, Performance enhancement of ZnSnP$_2$ solar cells by a Cu$_3$P back buffer layer, *Sol. Energy Mater. Sol. Cells*, 2021, **221**, 110891, DOI: 10.1016/j.solmat.2020.110891.

16 J. Li, Y. Huang, J. Huang, G. Liang, Y. Zhang, G. Rey, F. Guo, Z. Su, H. Zhu, L. Cai, K. Sun, Y. Sun, F. Liu, S. Chen, X. Hao, Y. Mai and M. A. Green, Defect Control for 12.5% Efficiency Cu$_2$ZnSnSe$_4$ Kesterite Thin-Film Solar Cells by Engineering of Local Chemical Environment, *Adv. Mater.*, 2020, **32**(52), 2005268, DOI: 10.1002/adma.202005268.

17 I. Suzuki, S. Kawanishi, T. Omata and H. Yanagi, Current status of n-type SnS: paving the way for SnS homojunction solar cells, *J. Phys. Energy*, 2022, **4**(4), 042002, DOI: 10.1088/2515-7655/ac86a1.

18 S. Niu, H. Huyan, Y. Liu, M. Yeung, K. Ye, L. Blankemeier, T. Orvis, D. Sarkar, D. J. Singh, R. Kapadia and J. Ravichandran, Bandgap Control via Structural and Chemical Tuning of Transition Metal Perovskite Chalcogenides, *Adv. Mater.*, 2017, **29**(9), 1604733, DOI: 10.1002/adma.201604733.

19 Y. Nishigaki, T. Nagai, M. Nishiwaki, T. Aizawa, M. Kozawa, K. Hanzawa, Y. Kato, H. Sai, H. Hiramatsu, H. Hosono and H. Fujiwara, Extraordinary Strong Band-Edge Absorption in Distorted Chalcogenide Perovskites, *Sol. RRL*, 2020, **4**(5), 1900555, DOI: 10.1002/solr.201900555.

20 X. Wei, H. Hui, C. Zhao, C. Deng, M. Han, Z. Yu, A. Sheng, P. Roy, A. Chen, J. Lin, D. F. Watson, Y.-Y. Sun, T. Thomay, S. Yang, Q. Jia, S. Zhang and H. Zeng, Realization of BaZrS$_3$ chalcogenide perovskite thin films for optoelectronics, *Nano Energy*, 2020, **68**, 104317, DOI: 10.1016/j.nanoen.2019.104317.

21 Z. Yu, H. Hui, D. West, H. Zhang, Y. Sun, S. Kong, Y. Zhang, C. Deng, S. Yang, S. Zhang and H. Zeng, Chalcogenide Perovskite Thin Films with Controlled Phases for Optoelectronics, *Adv. Funct. Mater.*, 2024, **34**(7), 2309514, DOI: 10.1002/adfm.202309514.

22 K. Hanzawa, S. Iimura, H. Hiramatsu and H. Hosono, Material Design of Green-Light-Emitting Semiconductors:

Perovskite-Type Sulfide SrHfS$_3$, *J. Am. Chem. Soc.*, 2019, **141**(13), 5343–5349, DOI: 10.1021/jacs.8b13622.

23 S. Maeda, Y. Tani, H. Katayama, D. Kanematsu, K. Oiwake, Y. Nishigaki, T. Miyadera, M. Chikamatsu, T. Nagai, T. Aizawa, K. Hanzawa, H. Hiramatsu, A. Terakawa, H. Hosono and H. Fujiwara, Enhancing analysis efficiency: Automation of spectroscopic ellipsometry for crystalline semiconductors and transparent conductive oxides, *Thin Solid Films*, 2023, **787**, 140099, DOI: 10.1016/j.tsf.2023.140099.

24 K. Hanzawa, T. Nagai, R. Nagasawa, T. Katase, H. Hosono and H. Hiramatsu, d^0 Cation-Based Spinel-Type Sulfide Semiconductors with Color-Tunable Direct-Gap and Ambipolar Dopability, *J. Am. Chem. Soc.*, 2025, **147**(39), 35935–35941, DOI: 10.1021/jacs.5c12816.

25 W. Shockley and H. J. Queisser, Detailed Balance Limit of Efficiency of *p-n* Junction Solar Cells, *J. Appl. Phys.*, 1961, **32**(3), 510–519, DOI: 10.1063/1.1736034.

26 A. Mahmood, S. M. Ramay, W. Al-Masry, A. A. Al-Zahrani and N. Y. A. Al-Garadi, Analyzing opto-electronic and transport characteristics of ZnSc$_2$Se$_4$ and CdSc$_2$Se$_4$ spinels for opto-electronic and energy storage devices, *Mod. Phys. Lett. B*, 2021, **35**(04), 2150184, DOI: 10.1142/S0217984921501840.

27 R. D. Shannon, Bond Distances in Sulfides and a Preliminary Table of Sulfide Crystal Radii, *Ind. Chem. Libr.*, 1981, **2**, 53–70, DOI: 10.1016/B978-0-12-525102-0.50009-8.

28 Z. Song and Q. Liu, Tolerance Factor and Phase Stability of the Normal Spinel Structure, *Cryst. Growth Des.*, 2020, **20**(3), 2014–2018, DOI: 10.1021/acs.cgd.9b01673.

29 M.-J. Choi, F. P. García de Arquer, A. H. Proppe, A. Seifitokaldani, J. Choi, J. Kim, S.-W. Baek, M. Liu, B. Sun, M. Biondi, B. Scheffel, G. Walters, D.-H. Nam, J. W. Jo, O. Ouellette, O. Voznyy, S. Hoogland, S. O. Kelley, Y. S. Jung and E. H. Sargent, Cascade Surface Modification of Colloidal Quantum Dot Inks Enables Efficient Bulk Homojunction Photovoltaics, *Nat. Commun.*, 2020, **11**(1), 103, DOI: 10.1038/s41467-019-13437-2.

30 G. S. Selopal, H. Zhao, Z. M. Wang and F. Rosei, Core/Shell Quantum Dots Solar Cells, *Adv. Funct. Mater.*, 2020, **30**(13), 1908762, DOI: 10.1002/adfm.201908762.

31 M. Hao, S. Ding, S. Gaznaghi, H. Cheng and L. Wang, Perovskite Quantum Dot Solar Cells: Current Status and Future Outlook, *ACS Energy Lett.*, 2024, **9**(1), 308–322, DOI: 10.1021/acsenergylett.3c01983.

32 J. Heyd, G. E. Scuseria and M. Ernzerhof, Hybrid Functionals Based on a Screened Coulomb Potential, *J. Chem. Phys.*, 2003, **118**(18), 8207–8215, DOI: 10.1063/1.1564060.

33 G. Kresse and J. Furthmüller, Efficient Iterative Schemes for Ab Initio Total-Energy Calculations Using a Plane-Wave Basis Set, *Phys. Rev. B: Condens. Matter Mater. Phys.*, 1996, **54**(16), 11169–11186, DOI: 10.1103/PhysRevB.54.11169.

34 G. Kresse and J. Furthmüller, Efficiency of Ab-Initio Total Energy Calculations for Metals and Semiconductors Using a Plane-Wave Basis Set, *Comput. Mater. Sci.*, 1996, **6**(1), 15–50, DOI: 10.1016/0927-0256(96)00008-0.

35 F. Izumi and K. Momma, Three-Dimensional Visualization in Powder Diffraction, *Solid State Phenom.*, 2007, **130**, 15–20, DOI: 10.4028/www.scientific.net/SSP.130.15.